Modeling hyperoxia-induced BOLD signal dynamics to estimate cerebral blood flow, volume and mean transit time

M. Ethan MacDonald [a,b,c,d,*], Avery J.L. Berman [a,b,c,d,e], Erin L. Mazerolle [a,b,c,d], Rebecca J. Williams [a,b,c,d], G. Bruce Pike [a,b,c,d,e]

[a] Department of Radiology, Calgary, AB, Canada
[b] Department of Clinical Neuroscience, Calgary, AB, Canada
[c] Hotchkiss Brain Institute, University of Calgary, Calgary, AB, Canada
[d] Seaman Family Magnetic Resonance Research Centre, Foothills Medical Centre, Alberta Health Services, Calgary, AB, Canada
[e] Montreal Neurological Institute, McGill University, Montreal, QC, Canada

ABSTRACT

A new method is proposed for obtaining cerebral perfusion measurements whereby blood oxygen level dependent (BOLD) MRI is used to dynamically monitor hyperoxia-induced changes in the concentration of deoxygenated hemoglobin in the cerebral vasculature. The data is processed using kinetic modeling to yield perfusion metrics, namely: cerebral blood flow (CBF), cerebral blood volume (CBV), and mean transit time (MTT). Ten healthy human subjects were continuously imaged with BOLD sequence while a hyperoxic (70% O_2) state was interspersed with baseline periods of normoxia. The BOLD time courses were fit with exponential uptake and decay curves and a biophysical model of the BOLD signal was used to estimate oxygen concentration functions. The arterial input function was derived from end-tidal oxygen measurements, and a deconvolution operation between the tissue and arterial concentration functions was used to yield CBF. The venous component of the CBV was calculated from the ratio of the integrals of the estimated tissue and arterial concentration functions. Mean gray and white matter measurements were found to be: 61.6 ± 13.7 and 24.9 ± 4.0 ml $100 \, g^{-1} \, min^{-1}$ for CBF; 1.83 ± 0.32 and 1.10 ± 0.19 ml $100 \, g^{-1}$ for venous CBV; and 2.94 ± 0.52 and 3.73 ± 0.60 s for MTT, respectively. We conclude that it is possible to derive CBF, CBV and MTT metrics within expected physiological ranges via analysis of dynamic BOLD fMRI acquired during a period of hyperoxia.

Introduction

Oxygen in air is inhaled through the lungs and diffuses into the blood where it binds with hemoglobin and is carried throughout the body for metabolic demands. The differential magnetic properties of oxy- and deoxy-hemoglobin enables functional MRI (fMRI) based upon blood oxygen level-dependent (BOLD) contrast technique. Hyperoxia was used to modulate venous deoxyhemoglobin concentration in the earliest BOLD fMRI paper (Ogawa et al., 1990). However, while the BOLD signal is very sensitive to cerebral blood flow (CBF) (Pike, 2012), it does not provide a quantitative measure of baseline perfusion. Arterial spin labelling (ASL) or dynamic susceptibility contrast (DSC) MRI, combined with kinetic modeling, are the primary MRI methods used to acquire this information. In this work, we propose using an inhaled oxygen increase and kinetic modeling of the BOLD time series for estimation of blood flow in the brain.

Compartmental modeling of blood flow in the brain has been extensively studied (Belliveau et al., 1990; Buckley, 2002; Buxton, 2009; Calamante et al., 2000; Chen and Pike, 2010; Frackowiak et al., 1980; Grubb et al., 1974; Lee, 2002; MacDonald and Frayne, 2015; MacDonald et al., 2011; Østergaard et al., 1996a, 1996b; Sourbron et al., 2009; Tofts, 1997; Tofts et al., 1999). Metrics related to cerebral perfusion include: incoming blood flow (cerebral blood flow, CBF), extravascular and intravascular (cerebral blood volume, CBV) spaces, and metabolic consumption of oxygen (cerebral metabolic rate of oxygen, $CMRO_2$). Oxygen is transported to the brain either bound to hemoglobin molecules in red blood cells or dissolved in the plasma of the blood (Severinghaus, 1979). Unlike most injected contrast agents, oxygen can pass freely through the blood-brain barrier from the intravascular space to the extravascular space because of its much smaller molecular size. When oxygen disassociates from hemoglobin in the red blood cells, the deoxygenated hemoglobin becomes paramagnetic and causes a reduction in T_2 and T_2^*; this effect is the basis of BOLD contrast (Ogawa et al., 1993). Any excess oxygen dissolved in blood plasma, such as during hyperoxia, will be consumed first leaving more hemoglobin bound with oxygen. Thus, while the dissolved oxygen itself does not have a significant direct effect
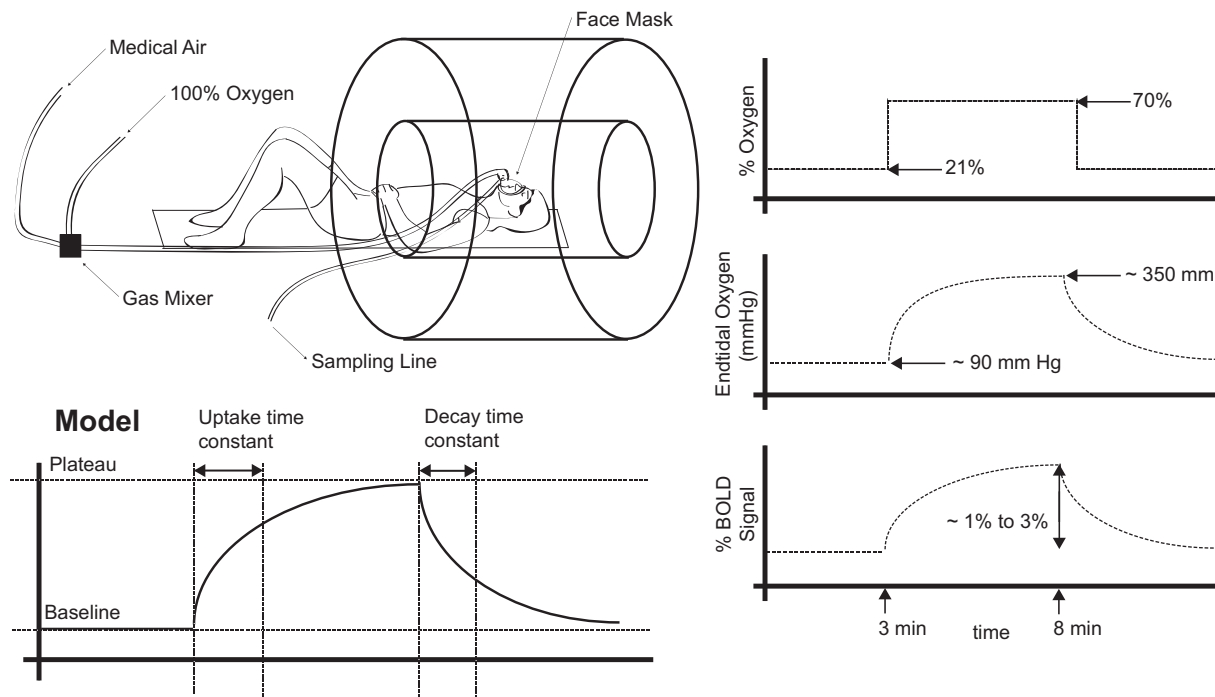
Fig. 1. Overview of experimental design and model. This diagram shows a high-level overview of the experiment. In the top left figure, the subject lays in the MRI bore wearing a non-rebreathing facemask. Connected to this facemask is a line of mixed incoming gases. Oxygen and carbon dioxide levels in the mask are continuously measured through a sampling line. In the top right figure, the effective percent of oxygen delivered during the course of the experiment is shown. In the next graph down, the expected end-tidal values are shown to slowly increase as the oxygen level in the lungs and blood becomes more saturated, and eventually plateaus at around 350 mm Hg partial pressure of oxygen. The BOLD signal also changes over time, but the uptake is delayed from that of the end-tidal values, as shown in the lower right-hand plot. In the bottom left-hand corner we show the exponential model used to parameterize both the end-tidal oxygen and BOLD signal time courses. The parameters characterized from our input signals include the baseline, plateau, uptake constant, and decay time constant.

on the BOLD signal (Berman et al., 2016; Ma et al., 2015), it indirectly has an effect by changing the oxygen saturation of the venous blood in direct proportion to the amount of dissolved oxygen delivered (*i.e.*, it decreases the amount of deoxygenated hemoglobin in the venous blood, hence increasing the BOLD signal). The changing concentration of deoxygenated hemoglobin is exploited in the current study to track the passage of a five-minute bolus of inhaled oxygen.

The kinetics of oxygen are tightly coupled to the kinetics of blood. Much can be understood about oxygen passage from previous studies examining the passage of blood through the brain (Frackowiak et al., 1980; Lee, 2002; Østergaard et al., 1996a, 1996b; Sourbron et al., 2009; Tofts, 1997; Tofts et al., 1999) and other inhalation experiments where gases enter the brain (Baron and Jones, 2012; Cui et al., 2013; Haddock et al., 2013). The methods used in these experiments vary greatly, and include: $^{15}O_2$ and $H_2^{15}O$ positron emission tomography (Frackowiak et al., 1980), arterial spin labeling (ASL) MR imaging (Alsop et al., 2015; Detre et al., 1992), contrast bolus passage imaging with computed tomography (Lee, 2002), and rapid T_1 and T_2*-weighted MR imaging of contrast bolus passage (Østergaard et al., 1996a, 1996b; Sourbron et al., 2004, 2009). In $^{15}O_2$ positron emission tomography studies, the uptake rate, CBF and $CMRO_2$ are obtained by monitoring the positron-emitting $^{15}O_2$. $H_2^{15}O$ positron emission tomography and ASL MR imaging measure the delivery of water, which also crosses the blood-brain barrier, but at a different rate than oxygen. Bolus passage imaging with either computed tomography, or T_1-or T_2*-weighted MR imaging use injected contrast agents that do not cross into the extravascular space, unless there is a pathological disruption in the blood brain barrier. In the bolus passage imaging experiments, linear time invariance is assumed in order to use a convolution model. Estimates of tissue perfusion metrics can be obtained by deconvolving the arterial input function from the tissue signals.

There are potential confounds with using oxygen as a contrast agent.

Oxygen is expected to cause mild constriction of the arteriole vessels at high concentrations (Bulte et al., 2006). There is also evidence to suggest that hyperoxia might induce hypercapnia (Grandin et al., 2005; Iscoe and Fisher, 2005) causing vasodilation and increasing the CBF, while more recent work suggests that an isocapnic hyperoxia prevents confounding changes in CBV (Croal et al., 2017). Gaseous oxygen, which is paramagnetic, has also been shown to induce magnetic field perturbations when high concentrations of oxygen are present in a face mask and sinuses (Pilkinton et al., 2011).

The effect of oxygen on the BOLD signal has been examined in several studies. Reported by Bulte et al. (2006) were signal changes at different baseline oxygen inhalation levels and end-tidal values. In 2012, Gauthier & Hoge and Bulte et al. proposed very similar methods for measuring oxygen extraction fraction (OEF) and $CMRO_2$ from a dual hypercapnia and hyperoxia stimulus (Bulte et al., 2012; Gauthier and Hoge, 2012). Further, studies have modeled the oxygen uptake with a first order exponential function and have shown differences across gray and white matter regions (Haddock et al., 2013). This was followed by work from Blockley et al. (2013) who used an oxygen stimulus to quantify venous CBV by measuring the steady-state BOLD signal change with hyperoxia. This current work builds on these experiments by modeling the BOLD signal dynamics during a period of increased inhaled oxygen on a voxel by voxel basis, and then applying a convolution model to estimate perfusion parameters. Specifically, we use T_2*-weighted BOLD imaging to rapidly measure the change in deoxygenated hemoglobin concentration caused by the passage of a 5-min bolus of increased oxygen. The BOLD time courses are fit to an exponential model and deconvolved from an arterial input function derived from the end-tidal partial pressure of oxygen, yielding information about the CBF. This technique is demonstrated in ten healthy human subjects and gray and white matter hemodynamic measurements are compared with literature values. Repeatability is also assessed in three subjects.
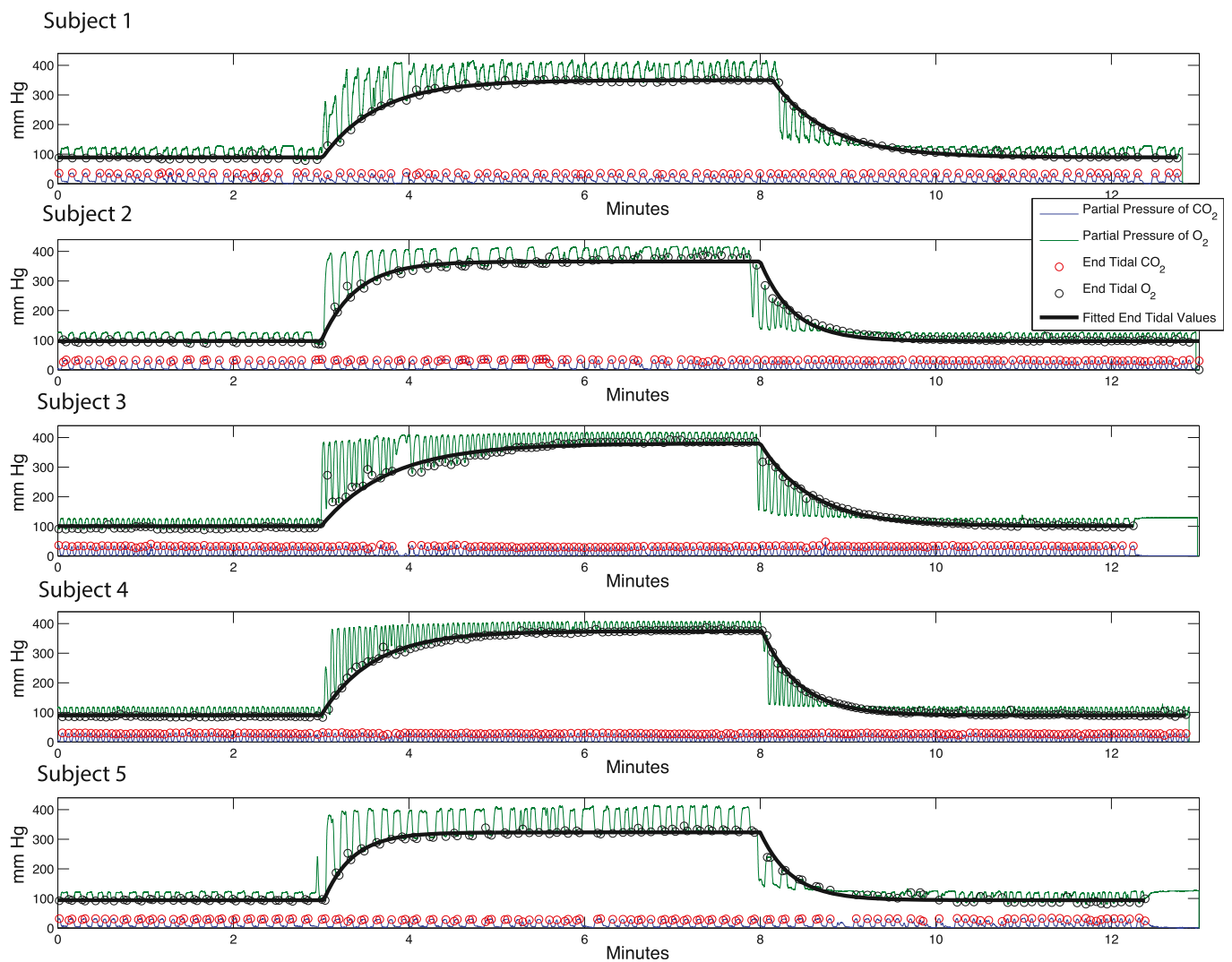
Fig. 2. Measured and modeled end-tidal gas concentrations. Here we show the time courses from five subjects during the oxygen stimulus. The green line shows the measured oxygen from the sampling line, and the blue line shows the measured carbon dioxide. The time corresponding to the local peak carbon dioxide is used to define the end-tidal gas pressures for both the carbon dioxide and oxygen, red and black circles respectively. The model fit of end-tidal oxygen values is shown with the black line.

Theory

A general overview of the experimental methodology is presented in Fig. 1. The technique uses signal from two sources: the end-tidal partial pressure of oxygen ($P_{ET}O_2$) and the T_2^*-weighted (BOLD fMRI) time series. The end-tidal partial pressure is a close approximation to the dissolved gas concentration in the arterial blood (Ito et al., 2008). If one knows the partial pressure of oxygen in the arterial blood (PaO_2), one can also calculate the oxygen saturation (SaO_2), the oxygen bound to red blood cells, and the total oxygen in the blood (Severinghaus, 1979). The change in the T_2^*-weighted BOLD signal is dominated by the concentration of deoxygenated hemoglobin. As the blood passes through the capillary bed, the excess dissolved oxygen is consumed first, leaving more oxyhemoglobin (less deoxyhemoglobin), and hence the BOLD signal increases (Bulte et al., 2006). Thus, while the delivered bolus of extra oxygen during a hyperoxia period is not directly detectable with BOLD fMRI while in the arterial phase, its presence is detectable in the post-arterial phase since the deoxyhemoglobin concentration will change in direct proportion to the delivered oxygen, assuming a fixed $CMRO_2$. Considering the change from a baseline condition of normoxia, the arterial oxygen input function is given by the $\Delta P_{ET}O_2$ and the venous oxygen output function is related to ΔBOLD.

Following a tracer kinetics modeling approach (Østergaard et al., 1996a, 1996b; Tofts, 1997; Tofts et al., 1999), the concentration of extra oxygen in the venous blood of the brain tissue, $C_T(t)$, can be related to the concentration of extra oxygen in the arterial input function, $C_A(t)$, with a linear time invariant convolution model. The normalized impulse response function $R(t)$ is scaled by CBF and the convolution is expressed as:

$$C_T(t) = CBF \, C_A(t) \otimes R(t) \tag{1}$$

The concentration of the oxygen in the arterial blood is estimated from the end-tidal oxygen measurement, which is equated to the dissolved oxygen, PaO_2,

$$C_A(t) = \varphi[Hb]SaO_2 + \varepsilon PaO_2 \tag{2}$$

where φ represents the O_2 carrying capacity of hemoglobin (1.34 ml O_2/g_{Hb}), and ε is the solubility coefficient of oxygen in blood (0.0031 mL_{O2}/(dL_{Blood} mm Hg)). The concentration of hemoglobin ([Hb]) is assumed to be 15 g Hb dL^{-1} blood. The relationship between SaO_2 and PaO_2 is given by the Severinghaus equation (Severinghaus, 1979),
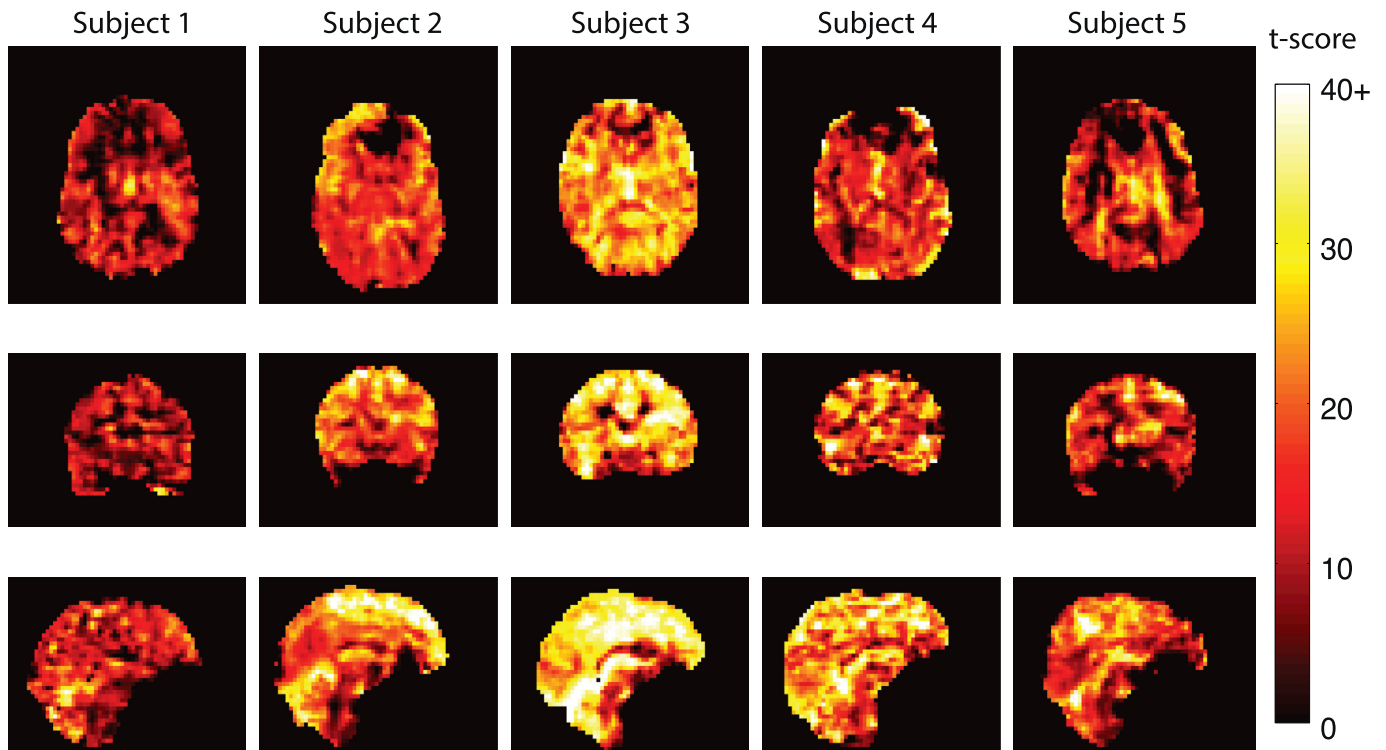
Fig. 3. Individual activation maps from the oxygen stimulus. These maps show the t-statistic output from a general linear model of the hyperoxia stimulus. Masks are thresholded at t > 2.3. Robust whole brain activation is observed. Slices are selected in three orthogonal planes through the center of the acquisition volume.

$$SaO_2 = \cfrac{1}{\left(\cfrac{23400}{(PaO_2)^3 + 150(PaO_2)} + 1\right)} \tag{3}$$

Given the BOLD signal's dependence on the concentration of deoxy-hemoglobin in venous blood and the complementary relationship between deoxyhemoblogin concentration and blood oxygenation, it is possible to determine the change in oxygen concentration in the venous blood of brain tissue using a calibrated fMRI model of the BOLD signal (Davis et al., 1998; Hoge et al., 1999),

$$\frac{\Delta S_{T2*}}{S_{T2*}|_0} \approx -TE\ A\ CBV\left([dHb]^\beta - [dHb]^\beta|_0\right) \tag{4}$$

Where $S_{T2*}|_0$ and $\Delta S_{T2*}(t)$ are the BOLD signal baseline and change, respectively, TE is the echo time, A is a scaler and β is a constant of 1.3 (Boxerman et al., 1995; Mark et al., 2011). Each hemoglobin can carry four O_2 molecules, the relationship between the oxygen concentration and deoxygenated hemoglobin concentration in partially deoxygenated blood is,

$$[O_2] = 4([Hb] - [dHb]) \tag{5}$$

Combining equations (4) and (5), and rearranging yields

$$[Hb] - \frac{[O_2]}{4} = \left(\frac{-1}{A\ TE\ CBV}\frac{\Delta S_{T2*}}{S_{T2*}|_0} + \left([Hb] - \frac{[O_2]|_0}{4}\right)^\beta\right)^{1/\beta} \tag{6}$$

To simplify, because we are interested in the relative concentration changes in oxygenation, so the hematocrit ([Hb]) and baseline oxygen ($[O_2]|_0$) are omitted, and because we are interested in the whole voxel and not just the fraction of blood, the CBV term is removed. The simplified relationship between the change in the oxygen concentration from

baseline, $C_T(t)$, and the change in BOLD signal is be approximated as:

$$C_T(t) = \left(\frac{1}{TE\ k_2}\frac{\Delta S_{T2*}(t)}{S_{T2*}|_0}\right)^{1/\beta} \tag{7}$$

where k_2 is a scaling coefficient derived empirically (see Methods). Once the concentration functions are obtained from the arterial blood and from the brain tissue signals, the convolution model (Eq (1)) can be utilized and solved through spectral division, yielding the CBF estimate,

$$CBF = \max\left[iDFT\left\{\frac{C_T(f)}{C_A(f)}\right\}\right] \tag{8}$$

Where iDFT is the inverse discrete Fourier transform operator and $C_T(f)$ and $C_A(f)$ are the Fourier transforms of $C_T(t)$ and $C_A(t)$, respectively.

CBV can be calculated from the ratio of the integrals of the tissue and arterial concentration functions. Scaled by the blood density, $\rho = 1.04\ g\ ml^{-1}$,

$$CBV = \frac{\int C_T(t)dt}{\rho \int C_A(t)dt} \tag{9}$$

This method is similar to that described by Rempp et al., (Rempp et al., 1994), except that it does not require scaler in the numerator to account for hemocrit differences between the large and small vessels because of the use of oxygen in this experiment instead of gadolinium contrast agent.

The final parameter that we estimate is the mean transit time (MTT) which represents the average time that a particle takes to pass through the observation compartment. It is found by taking the ratio of CBV and CBF.
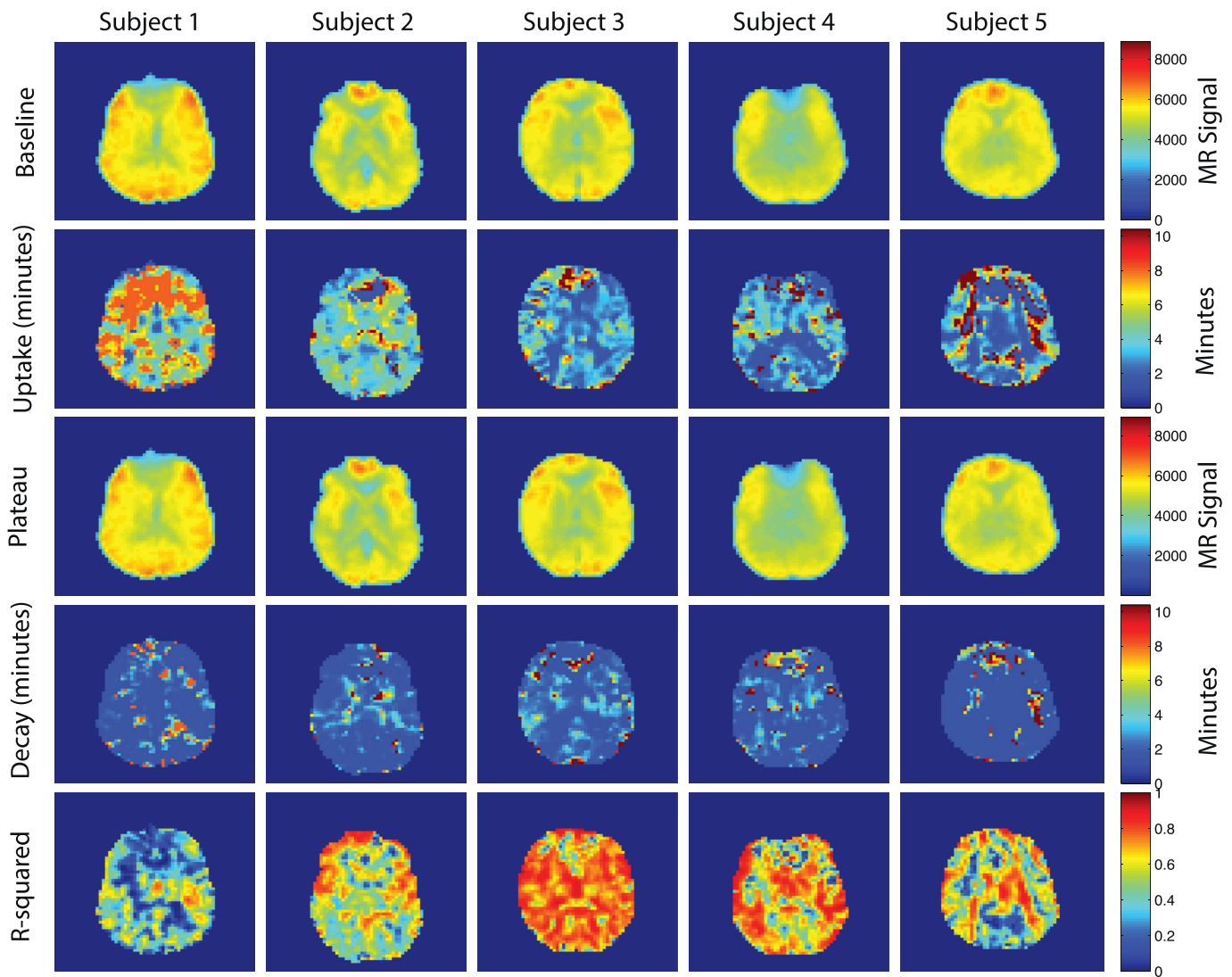
Fig. 4. Parametric maps. From the fitting process we obtain maps of the baseline and plateau levels, as well as the uptake and decay time constants. The R^2 maps, which illustrate the quality of fit, are shown in the bottom row.

Methods

Data acquisition

Imaging was performed on a 3T MR scanner (Discovery 750, GE Healthcare) with a 12-channel neurovascular head coil. A respiration apparatus was used for manipulating inhaled gases during scanning (Fig. 1). A non-rebreathing facemask connected to a dual-limb airway was fitted with unidirectional valves to ensure distinct delivery and sampling of expired gases. Automatic gas delivery was achieved using a custom-built system that consisted of a Digital Flo-Box and Mass Flow Controllers (Sierra Instruments, Monterey, CA) for gas delivery and Biopac sampling equipment (Modules: TSD160A, C02100C, O2100C, and MP150 DAC; BIOPAC Systems Inc., Goleta, CA) for continual recording of expired gases (CO_2 and O_2). The gas states used were medical air (21% oxygen and 79% nitrogen) and a mixture of medical air and oxygen (70% oxygen and 30% nitrogen). The study was approved by our institutional Research Ethics Board and all 10 subjects provided informed written consent.

To ascertain the potential changes in CBF and induced macroscopic field perturbations (e.g. around sinus cavities) between these gas states, three subjects were imaged using phase contrast (PC) imaging, arterial spin labeling (ASL), and a multi echo gradient recalled echo sequence (used for B_0 mapping). For this part of the experiment, an equilibrium state was achieved with the new gas levels before imaging and maintained throughout the acquisition. The PC parameters were TR/TE/α of 8.3 ms/3.8 ms/10°, a matrix acquisition size of $256 \times 192 \times 192$ over a $22.0 \text{ cm} \times 16.5 \text{ cm} \times 19.2 \text{ cm}$ field-of-view, and a velocity encoding of $v_{enc} = 150 \text{ cm s}^{-1}$. The PC acquisition took 10 min 40 s. Measurements of volume flow rate were obtained from the PC data at major cerebral artery segments and compared between states. A pseudo-continuous ASL sequence was used with a labeling duration and a post-labeling delay time of 1.0 s and 2.5 s, respectively. A 3D stack of spirals readout trajectory was used with a slice thickness of 4 mm. The spiral had a readout bandwidth of 62.5 kHz and acquired 1024 points per arm, and 4 total arms per slice, yielding an effective resolution of 3.3 mm^2 in-plane. The ASL sequence took 4 min 21 s. CBF was quantified using the algorithm outlined in (Alsop et al., 2015), and corrected for deviation in blood T_1 during the hyperoxia stimulus (blood T_1 of 1.60 and 1.66 s for normoxia and 70% hyperoxia, respectively (Pilkinton et al., 2012)). Measurements of CBF were then compared between gas states. For B_0 mapping a multi echo gradient recalled echo sequence was used with TR/α of 29.8 ms/20° and a unipolar eight-echo train with TEs of 3.912 ms–26.656 ms separated by 2.632 ms. The acquisition had a field of view of $25.6 \text{ cm} \times 19.2 \text{ cm} \times 12.8 \text{ cm}$ with a matrix acquisition size of $256 \times 192 \times 128$, yielding 1 mm^3 resolution. Sensitivity encoding with

Concentration Functions
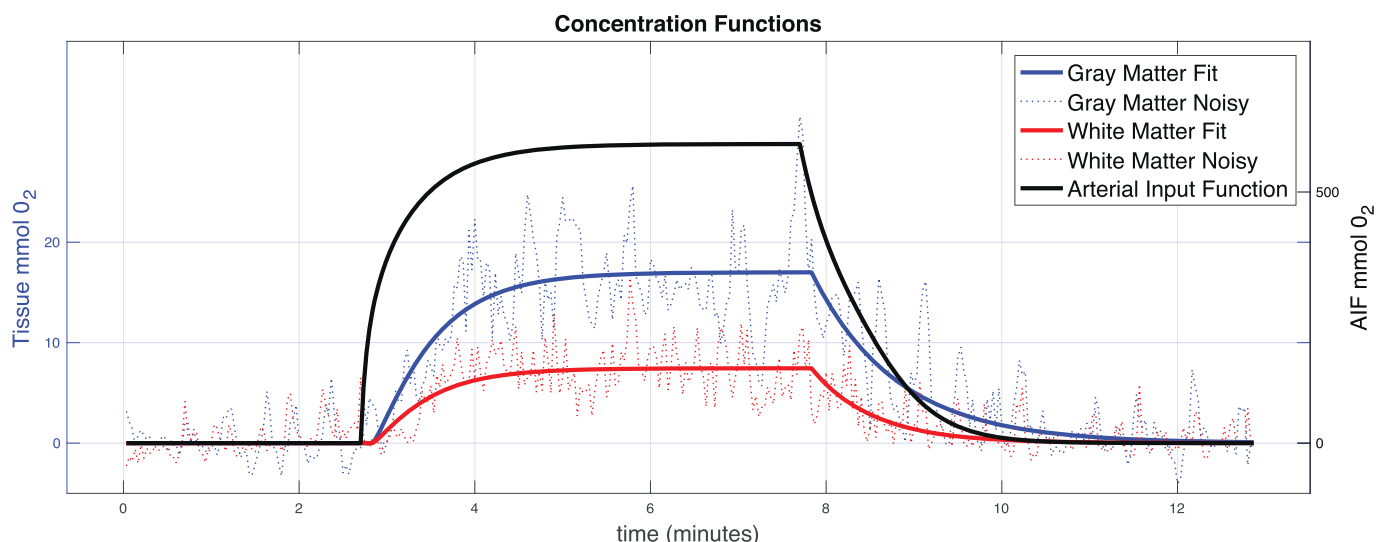
Fig. 5. Example AIF, gray and white matter concentration functions. AIF represents the concentration of extra oxygen from the stimulus in the arterial blood (right axis), and the other two curves show the fitted function from representative gray and white matter voxels (left axis). As expected, a fast uptake is observed in the AIF and delayed uptake is observed in gray matter with slightly greater delay of the uptake in white matter. The dashed lines indicated the noisy signal from the individual voxels where the measurements were taken.
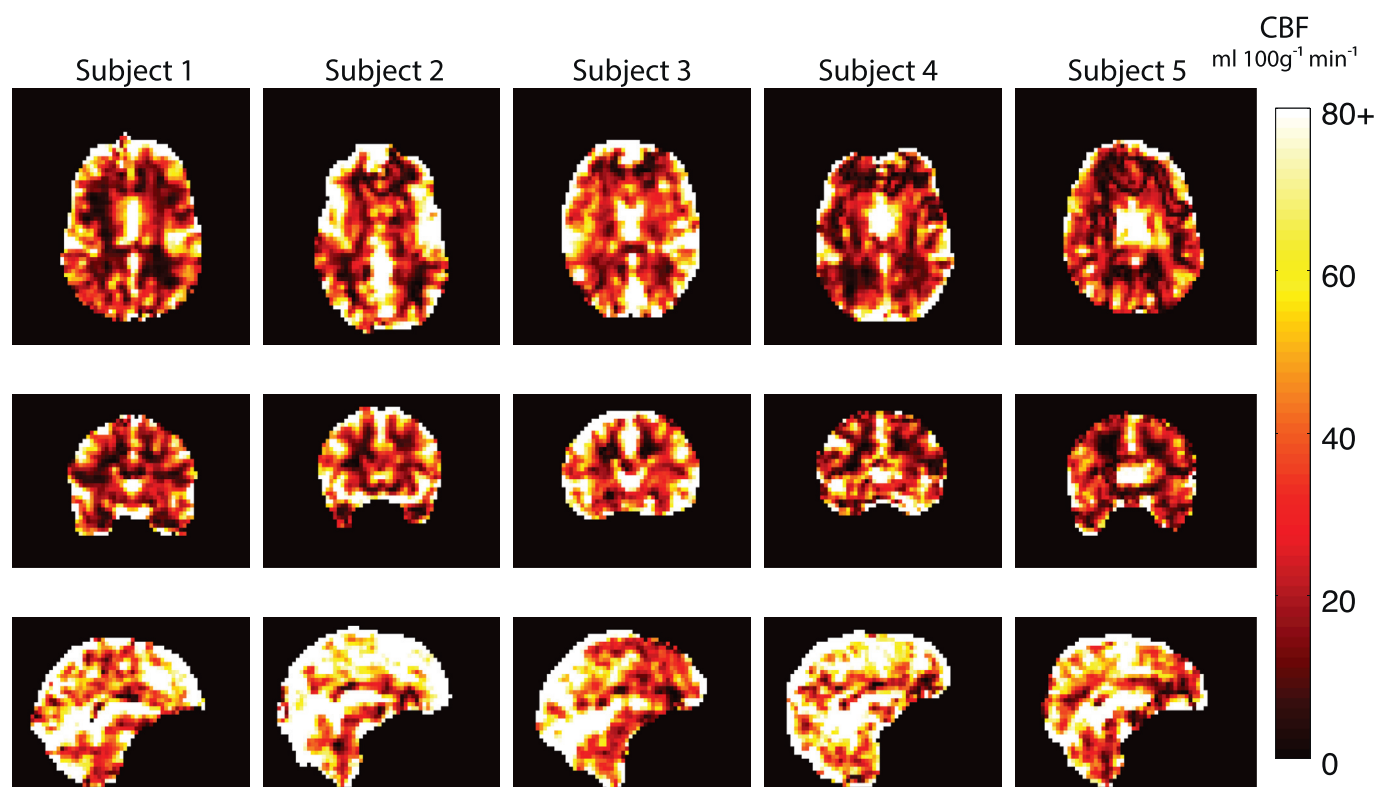
Fig. 6. Cerebral blood flow (CBF) maps. Good conspicuity between gray and white matter is observed on the axial (top row) and coronal (middle row). The sagittal images (bottom row) show high flow, as these images contain large draining veins and high blood volume.

an acceleration factor of 2 allowed a scan time of 4 min 20 s. The B_0 field was calculated by fitting the phase evolution between the echoes, and these fields were compared between gas states. The results of these findings about the confounds, CBF and B_0, can be found in the supplemental data.

T1-weighted anatomical scans were acquired for the purposes of registration and segmentation. A T1-weighted magnetization prepared gradient echo sequence was used, with TI/TR/TE/flip of 650 ms/6.6 ms/ 2.9 ms/10°, and field of view of $256 \times 256 \times 192$ with 1 mm isotropic resolution. Gradient-echo echo planar images (EPI) were collected in all ten subjects in order to observe the BOLD signal changes in the brain. The EPI acquisition parameters were TR/TE/flip of 2000 ms/30 ms/80° with an in-plane matrix of 64×64, over a 224 mm $\times$ 224 mm field-of-view. Forty-three slices (3.5 mm thick) were collected with an interleaved
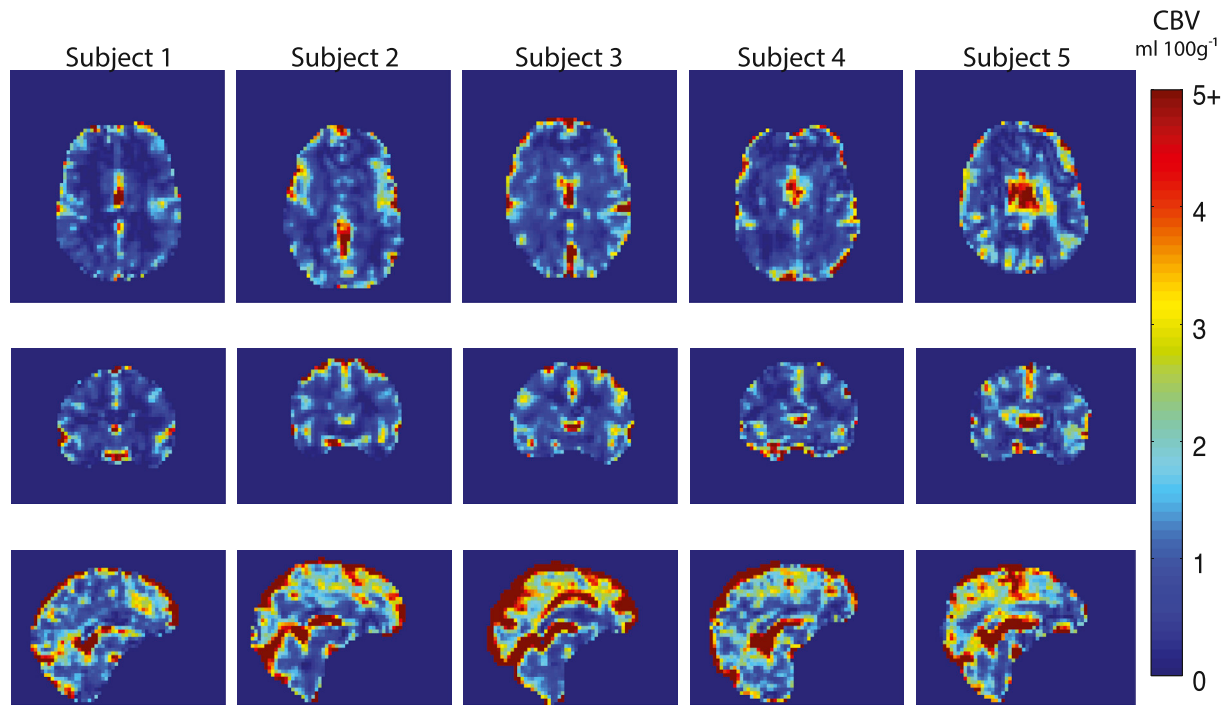
Fig. 7. Venous cerebral blood volume (CBV) maps. Particularly high blood volume along the midline corresponds to where major draining veins are located.
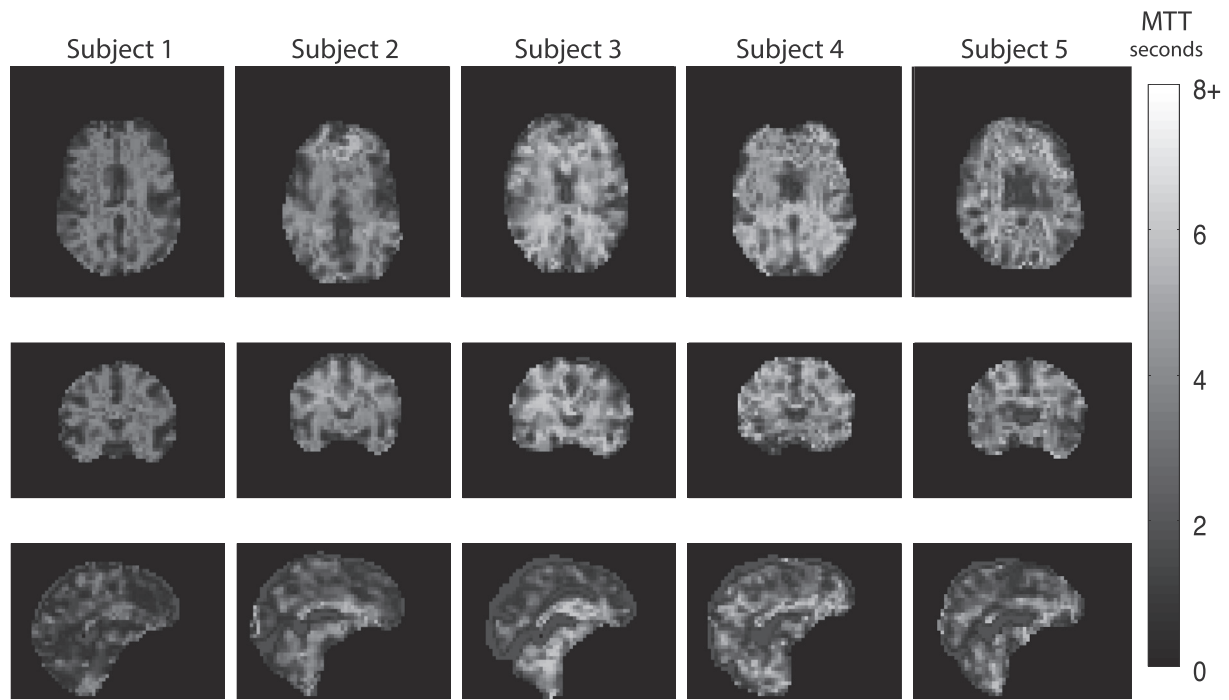
Fig. 8. Mean transit time (MTT) maps. MTT is calculated as the ratio between the CBV and CBF.

Table 1
Individual and group averages of perfusion parameters. Values are reported as mean ± standard deviation.

	CBF (ml 100 g^{-1} min^{-1})		CBV (ml 100g^{-1})		MTT (seconds)	
	GM	WM	GM	WM	GM	WM
Subject 1	79.2 ± 31.5	29.0 ± 17.1	1.68 ± 0.71	0.92 ± 0.35	2.03 ± 0.98	2.89 ± 0.99
Subject 2	53.3 ± 26.2	24.0 ± 16.0	1.79 ± 0.73	1.13 ± 0.48	2.84 ± 1.18	3.64 ± 1.13
Subject 3	82.9 ± 36.8	28.5 ± 20.3	2.17 ± 0.92	1.22 ± 0.48	3.20 ± 1.39	4.26 ± 1.28
Subject 4	72.2 ± 31.5	30.1 ± 18.9	2.09 ± 0.90	1.19 ± 0.53	3.29 ± 1.41	4.10 ± 1.26
Subject 5	44.6 ± 24.0	21.2 ± 13.6	2.06 ± 0.79	1.42 ± 0.55	2.82 ± 1.24	3.54 ± 1.26
Subject 6	54.3 ± 28.3	20.6 ± 14.2	1.42 ± 0.67	0.85 ± 0.37	2.53 ± 1.07	3.21 ± 0.95
Subject 7	66.5 ± 29.7	26.0 ± 16.8	2.19 ± 0.88	1.25 ± 0.53	3.69 ± 1.40	4.63 ± 1.18
Subject 8	66.9 ± 32.4	28.3 ± 20.4	1.27 ± 0.48	0.83 ± 0.31	2.60 ± 1.05	3.19 ± 0.90
Subject 9	46.2 ± 23.6	21.6 ± 13.4	1.68 ± 0.68	1.09 ± 0.45	2.76 ± 1.21	3.40 ± 1.12
Subject 10	50.0 ± 26.7	19.4 ± 13.7	1.92 ± 0.84	1.10 ± 0.47	3.65 ± 1.46	4.43 ± 1.23
Average	**61.6 ± 13.7**	**24.9 ± 4.0**	**1.83 ± 0.32**	**1.10 ± 0.19**	**2.94 ± 0.52**	**3.73 ± 0.60**

slice order. A total of 390 vol were collected with a scan time of 13 min during the dynamic gas stimulus (3 min normoxia, 5 min hyperoxia, 5 min normoxia). In three of the subjects, the BOLD scan was performed twice to determine the repeatability of the method.

Data pre-processing

All pre-processing, modeling, and analysis were performed with purpose-built code using MATLAB (The MathWorks, Natick, MA) except for registration and segmentation, which were performed with ANTs (Advanced Normalization Tools). Pre-processing of the end-tidal values included: correcting for minor delays between the CO_2 and O_2 recordings; calculation of the autocorrelation between the CO_2 and O_2 time courses from the baseline portion of acquisition; and correcting the delay for the whole series. The local maxima on the CO_2 trace were used throughout the duration of the hyperoxia run to determine the end-tidal points. Pre-processing of the BOLD data included motion correction and spatial smoothing with a 5 mm FWHM Gaussian kernel. Brain extraction was performed on the anatomical scans of each subject and then the tissues were segmented into three tissue types with a k-means classifier with priors. Rigid-body registration was used to align the mean BOLD volume with the anatomical acquisition. A transformation was calculated in order to align data in the anatomical space to the ICBM atlas (Mazziotta et al., 2001) and calculate a group average map.

Kinetic modeling

After preprocessing, the BOLD image data was fit to a piece-wise exponential response model (Fig. 1, bottom left), which had four parameters: the normoxic baseline, the hyperoxic plateau, the uptake time constant, and the decay time constant. Additionally, the exponential response model included linear and quadratic signal terms to remove drift artifacts from the BOLD signal. Fitting was performed with initial conditions based on the geometry of the BOLD signal (*i.e.*, the baseline signal was initially estimated to be the average of the first three minutes). A conjugate gradient fitting algorithm was used to minimize the root mean square (RMS) error between the model and the BOLD time series. Maps of each of the parameters were generated and the coefficient of determination (R^2) was calculated for the fitted curves to assess the quality of the fitting process.

Eqs. (2) and (3) were used along with the $P_{ET}O_2$ measurements to determine the total arterial concentration of oxygen over time. This concentration function was then used as the arterial input function, $C_A(t)$, for modeling the passage of oxygen through the brain. The k_2 constant in Eq (7) was established to be ~0.2 by scanning an additional three subjects and finding the k_2 that yielded the expected concentration of oxygen (120 mL$_{O2}$/L$_{Blood}$); when this empirically estimated k_2 was applied to the ten subjects used in the main analysis it provided consistent results. The tissue signals came from the BOLD image data and the tissue concentration of oxygen, $C_T(t)$, was calculated using Eq. (7). Next, the

concentration functions were resampled from fitted parameters. This allowed uniform samples of an end-tidal time course matching the sampling of the BOLD times series, and the BOLD time series were resampled from the fitted model with the drift term removed. With the concentration functions, the deconvolution operation was performed (Eq. (8)) using a low pass filter with a cutoff frequency of 10 Hz to stabilize the spectral division (MacDonald et al., 2011). The peak of the impulse response was determined to be the CBF. The CBV_V measurement was calculated using Eq (9). Mean transit time (MTT) was calculated as the ratio between CBV_V and CBF.

Analysis

To restrict our analysis to regions with a statistically significant BOLD response to the hyperoxia stimulus, t-statistic maps were computed using the general linear model. A boxcar model of the 3-5-5 min paradigm was convolved with a single gamma response function having a full width at half maximum of 60 s (Bulte et al., 2012; Poulin et al., 1996). This broader distribution (relative to a typical hemodynamic response function) was used to accommodate the slow uptake of oxygen (Haddock et al., 2013). t-maps were computed to confirm the hyperoxia response. A mask was calculated by removing all voxels with t-statistics < 2.3 to exclude voxels with non-significant responses. The intersection of this mask and the gray and white matter regions was computed from the ICBM atlas. Using these regions, average gray and white matter parameters were obtained from the perfusion estimates.

Results

End-tidal response

Fig. 2 shows the continuously measured partial pressures of CO_2 and O_2, as well as the end-tidal points and model fit. Fitting of the exponential uptake and decay model to the end-tidal values was very robust (R^2 ranging from 0.983 to 0.998, with an average R^2 of 0.989). The average baseline values of $P_{ET}O_2$ were 97.6 ± 5.6 mm Hg (ranging from 88.9 mm Hg to 105.9 mm Hg), and the average plateau was of $P_{ET}O_2$ 370.5 ± 20.1 mm Hg (ranging from 323.1 mm Hg to 388.2 mm Hg). The average uptake time constant was 152.0 ± 45.3 s (ranging from 77.6 s to 212.3 s). The decay constants were similar to the uptake constants, the average was 161.9 ± 38.4 s (ranging from 95.4 s to 217.1 s). The average $P_{ET}CO_2$ values for the normoxia and hyperoxia states were 29.4 ± 3.0 mm Hg and 29.9 ± 2.8 mm Hg respectively; this difference was not statistically significant.

Confounds of oxygen stimulus

The volume flow rate, CBF and B_0 measurements were significantly correlated between the normoxia and hyperoxia states ($p < 0.001$), these results can be found in the supplemental data. Key linear fits and
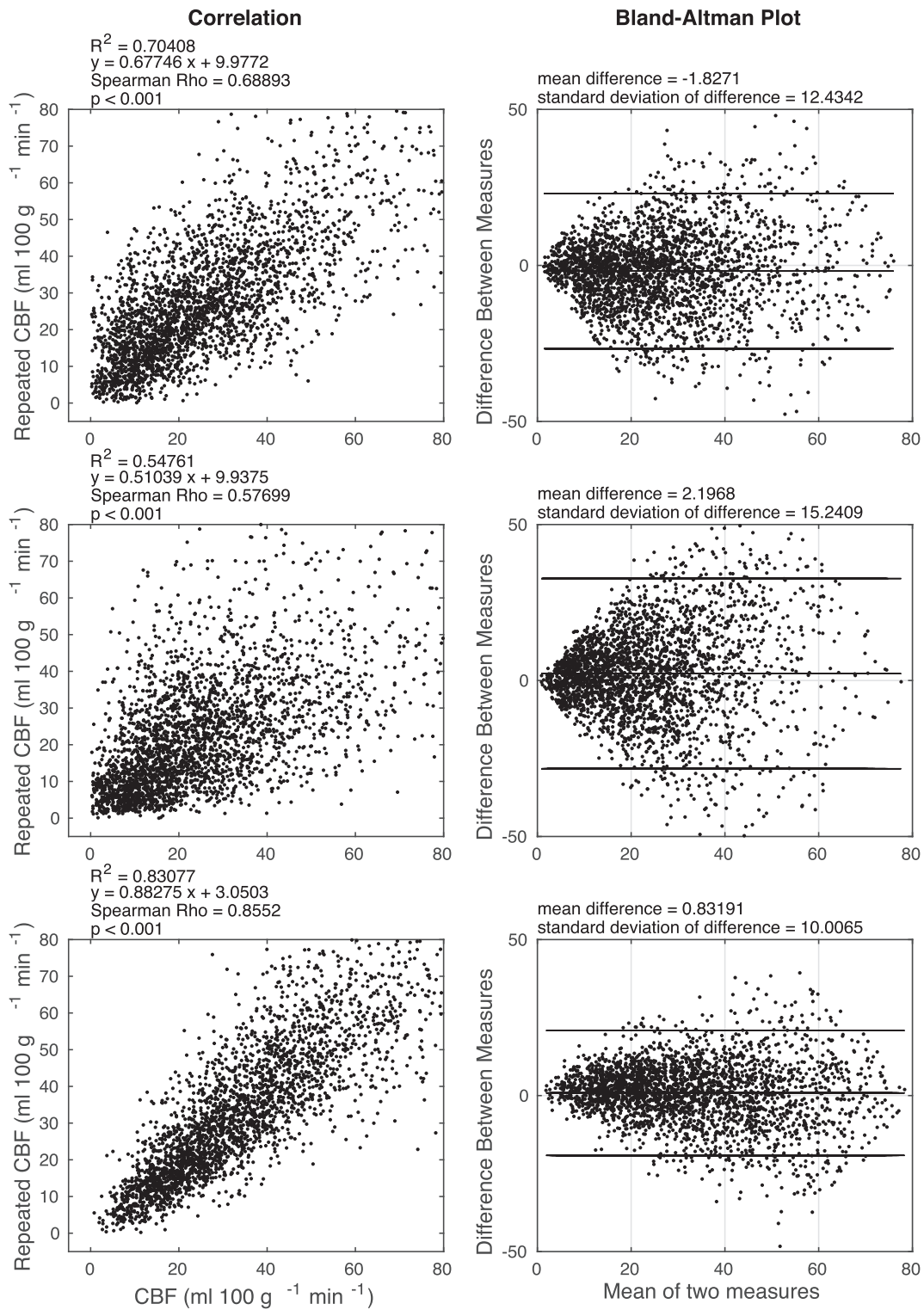
Fig. 9. Repeatability analysis. Three subjects were scanned twice and the CBF measurements were calculated for each. Voxel-wise Bland-Altman analysis is used to assert reliability.

correlation parameters were found to be: $y = 0.745x + 0.963$, $R^2 = 0.803$, $\rho = 0.701$ for PC; $y = 0.947x + 1.798$, $R^2 = 0.925$, $\rho = 0.928$ for ASL; and $y = 0.971x + 0.021$, $R^2 = 0.931$, $\rho = 0.968$ for B_0 mapping (x is the normoxia data and y is the hyperoxia data). Bland-Altman analysis showed small mean differences between gas states, for PC: 0.58 ± 1.06 ml/s; for ASL: 0.88 ± 7.85 ml $100\,g^{-1}\,min^{-1}$; and for B_0 maps: -0.02 ± 0.43 mT. All three data types therefore showed significant but very small effects of the 70% oxygen stimulus used in this experiment.

Stimulus effect

Statistical maps of BOLD response to hyperoxia are shown in Fig. 3 indicating a robust response to the hyperoxia stimulus. In gray and white matter regions, the t-score values were found to be 18.1 ± 6.8 and 16.3 ± 5.8, respectively (mean $\pm$ standard deviation). The binary masks calculated from the statistical maps included most of the gray and white matter but excluded regions where the signal was attenuated from

Group Average Maps
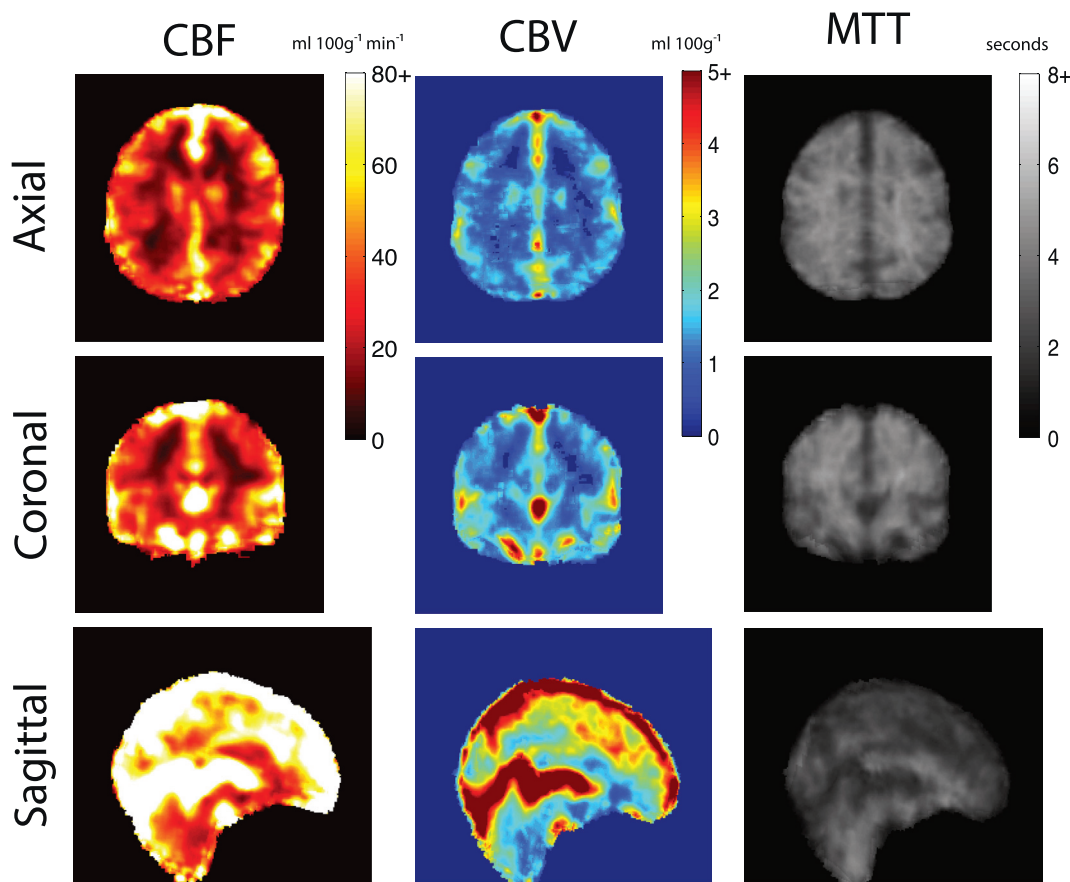
Fig. 10. Group average maps of CBF, CBV and MTT showing mid plane of the ICBM in the axial, sagittal and coronal orientations.

susceptibility, such as around the nasal sinus and ear canal. In Fig. 4, images of the model parameters, which characterize the BOLD signal at each voxel, are shown. The mean uptake time constants in gray and white matter were found to be 1.65 ± 0.54 and 1.78 ± 0.66 min, respectively, when averaged across all subjects, while the decay time constants were 1.41 ± 1.13 and 1.45 ± 1.14 min.

Model fitting

The fit parameters (baseline, plateau, uptake and decay times) and the quality of fit are shown in Fig. 4. Regions of low R^2 tended to correspond to regions of low t-values on the t-statistic maps (Fig. 3). Using 1st & 2nd order drift correction and fixing the stimulus on and off times, rather than fitting for them, both substantially improved the quality of the model fits (data not shown).

In Fig. 5, example modeled concentration functions are shown for the AIF, gray matter and white matter signals. The baseline oxygen is subtracted in this case and we only plot the change in oxygen content relative to the baseline physiological levels. These concentration curves resemble the amplitude ratios of concentration curves found from other bolus tracking experiments (Calamante et al., 2000; MacDonald and Frayne, 2015; Sourbron et al., 2007, 2009; Sourbron and Buckley, 2011). As expected, the AIF oxygen concentration is larger than the tissue signals, and the gray matter is larger than the white matter.

Perfusion parameters

The CBF maps (Fig. 6) show contrast between gray and white matter

ranging from a ratio of 2.1–2.9, with a mean and standard deviation of 2.5 ± 0.3. CBF values were close to the expected values found in literature ($60 \text{ ml } 100 \text{ g}^{-1} \text{ min}^{-1}$ in gray matter and $22 \text{ ml } 100 \text{ g}^{-1} \text{ min}^{-1}$ in white matter) (Calamante et al., 2000; Hatazawa et al., 1995; Østergaard et al., 1996a, 1996b; Roberts et al., 2002; Sourbron et al., 2009). Our measurements, averaged across participants, were $61.6 \pm 13.7 \text{ ml } 100 \text{ g}^{-1} \text{ min}^{-1}$ in gray matter and $24.9 \pm 4.0 \text{ ml } 100 \text{ g}^{-1} \text{ min}^{-1}$ in white matter.

The CBV_V maps (Fig. 7) were about half what we expect to find for total CBV, based on the literature (Blockley et al., 2013; Calamante et al., 2000; MacDonald and Frayne, 2015; Sourbron et al., 2009). Literature values for total CBV are approximately $5 \text{ ml } 100 \text{ g}^{-1}$ in gray matter and $1.75 \text{ ml } 100 \text{ g}^{-1}$ in white matter. The group-averaged CBV_V values that we measured were $1.83 \pm 0.32 \text{ ml } 100 \text{ g}^{-1}$ in gray matter and $1.10 \pm 0.19 \text{ ml } 100 \text{ g}^{-1}$ in white matter and are within expected physiological ranges for venous blood volume. CBV_V map generation was robustly demonstrated in all subjects; although in regions where the statistical maps did not show a strong effect of the stimulus, lower than expected values were observed.

Mean transit time (MTT) maps (Fig. 8), which are the ratio of CBV to CBF, were also close to what is expected from literature values (Calamante et al., 2000). From those studies, we expect MTTs of 4.0 s in gray matter and 4.8 s in white matter through the entire arteriole and venule compartments. We expect the passage to be relatively slower on the venule side than the arterial side, which should yield MTT values a bit greater than half of the full compartment. In this study, average values were measured to be 2.94 ± 0.52 and 3.73 ± 0.60 s, respectively. A summary of perfusion parameters for gray and white matter regions is shown in Table 1.

The voxel-wise repeatability analysis comparing three subjects is presented in Fig. 9. Spearman correlation was used as a conservative indicator as the data was not normally distributed. All correlations were statistically significant ($p < 0.001$), with R^2 values of 0.70, 0.55 and 0.83, and the Spearman rho coefficient was 0.69, 0.57, and 0.86; which demonstrated a good to excellent repeatability. The mean difference of the Bland-Altman analysis was small relative to the standard deviation of the difference of measurements, further indicating consistent repeatability with noise from a non-bias source (see Fig. 10).

Discussion

The theory and methodology presented here demonstrate a new way to obtain perfusion estimates using BOLD imaging during a hyperoxia stimulus block. With this technique, we undertook the modeling of an extended bolus of oxygen dissolved in plasma, which manifests itself as an increased oxygen concentration bound to red blood cells in the post-arteriolar vasculature. The increase in delivered O_2, which has a negligible effect on the BOLD signal (Berman et al., 2016; Ma et al., 2015), was measured via end-tidal respiratory sampling and used as the arterial input function for kinetic modeling. BOLD fMRI was used to monitor the passage of the additional O_2 through the capillary bed, which appears as a signal increase due to the increase in oxygen bound to hemoglobin. This is different than PET $^{15}O_2$ imaging or $^{17}O_2$ MR imaging where the oxygen is the source of the signal (Hoffmann et al., 2014; Zhu et al., 2013a, 2013b).

In equation (7), the constant k_2 is introduced and was experimentally estimated in an independent group of subjects to be ~0.2. It is expected that this parameter will change with field strength, hemoglobin concentration of the blood, receiver coil configuration, and the assumed value of Beta. It is analogous to the constant used in DSC MRI where it is accepted that an absolute value is unknown (Willats and Calamante, 2012). The constant is a function of several aspects of Eq (6) including the scaling term 'A' from calibrated fMRI. A value of 0.2 was determined to produce the expected oxygen concentration in three test subjects. When 0.2 was applied to the 10 subjects included in this paper we found that it provided consistent estimates of the oxygen concentration functions.

This method requires several assumed values, which include: 1) the baseline oxygen extraction fraction and baseline venous oxygen concentration; 2) the coefficients used in the Serveringhaus equation: ε, ϕ, and the concentration of hemoglobin (hematocrit); 3) the calibrated fMRI values β and A (the scaling coefficient) (Davis et al., 1998; Hoge et al., 1999); and 4) the equivalence of $P_{ET}O_2$ and PaO_2 (Ito et al., 2008). Several equations were used in the modeling, including the CBV signal intensity relationship [Eq (9)], the convolution model [Eq (1)], and the Severinghaus equation [Eq (2)&3]. Some of these assumptions might be imprecise or vary with pathology. For example, the assumption equating $P_{ET}O_2$ and PaO_2 has been demonstrated in humans with standard atmospheric pressures and holds well under many conditions such as varied exercise excretion (Bengtsson et al., 2001), but cases of blood disorders (sickle cell enema, blood cancers, etc.), respiratory conditions (emphysema, chronic occlusive pulmonary disease, etc.), or experiments run under non-standard atmospheric pressure ranges, might violate this assumption. However, the values and relationships we used have been widely reported and used in the literature (Blockley et al., 2013; MacDonald et al., 2011; Severinghaus, 1979; Tofts, 1997; Tofts et al., 1999). A full sensitivity analysis examining the effects of all the parameters is left for future work.

Some recent work has suggested that arterial constriction occurs when delivering high concentrations of oxygen (Bulte et al., 2006; Pilkinton et al., 2012; Zaharchuk et al., 2008). We had concerns about the hyperoxia stimulus decreasing CBF and therefore selected a 70% oxygen mixture which produced a robust BOLD response but a negligible CBF changes, as measured with ASL and phase contract MRI (supplemental data). A 100%-hyperoxia stimulus would certainly create a larger BOLD signal change but an accompanying CBF change would confound the experiment. Arterial constriction was one part of the reasoning to not use a 100% oxygen stimulus, but another reason was to avoid large susceptibility effects from oxygen gas (paramagnetic) in the sinuses and vicinity of the mask that the subject was breathing through (Pilkinton et al., 2011). We did observe some susceptibility effects in the anterior-inferior region of the frontal lobe at 70% O_2, but it did not significantly affect the data quality. Supplemental data also shows that throughout the remainder of the brain the susceptibility induced field change was negligible between the gas states.

When performing task-based BOLD fMRI with stimuli presented in block experimental paradigms, multiple epochs of shorter duration (~15–30 s) are often performed and averaged together to improve signal detection. The length of the epochs are typically motivated by the length of the hemodynamic response function. We selected the 3-5-5 min paradigm as the uptake response to oxygen is much longer (~1 min) than the hemodynamic response function to a task (~5 s), so effective estimation of the plateau from an exponential decay requires a hyperoxia duration of 3–5 min.

The signal characteristics presented in this experiment have fundamental differences from other bolus passage experiments performed with injections. When performing an inhalation bolus passage experiment there is a much longer uptake delay than when the contrast agent is injected directly into the blood because of the longer time associated with the gas state reaching equilibrium in the lungs. With MRI contrast agent injections, the AIF is typically derived from a voxel in a large vessel containing incoming blood, but this tends to be a difficult and noisy measurement. In the deconvolution process, the noisy AIF results in instabilities (Chen et al., 2005a; MacDonald et al., 2011). Having a short bolus (ideally approximating a Dirac delta function) is desirable because the AIF then has a broad frequency spectrum and is better able to estimate higher frequency coefficients in the tissue residue function. In our hyperoxia experiment, the measured $P_{ET}O_2$, which is closely related to the oxygen in blood (Ito et al., 2008), was used to derive the AIF. This AIF is thus much broader in the time domain, and much narrower in the Fourier domain. However, the deconvolution instability problem expected with a broad AIF is mitigated, to a large extent, by the fact that the end-tidal signal has a very high SNR and is very well fit by an exponential model, which forms a very stable AIF for deconvolution. This is further buttressed by model fitting the BOLD signals. Finally, the higher number of samples, relative to the response time course, aids the model fitting.

There is more than one way to calculate the CBV from the data collected in this experiment. Here, we used the approach of previous DSC bolus tracking techniques with CBV calculated as the ratio of the area under the AIF and the tissue contrast time course (Chen et al., 2005b; Duhamel et al., 2006; Rempp et al., 1994). An alternative method for calculating CBV by scaling the difference between the normoxia and hyperoxia states by the method outlined by Blockley et al. (2013) which was derived through simulations. Although, using only the measured difference of the MR signal from the stimulus is robust, especially with such a long stimulus duration time, we opted to use the bolus ratio method. We note that if the method of Blockley et al. were used to estimate CBV within our proposed framework, the beta value used here (1.3) would need to adjusted to match that used by Blockley (1.0).

There are several ways to obtain perfusion metrics as described in the introduction. These methods vary greatly and although they can each provide similar quantitative CBF measurements, there are nuances that can cause them to vary under different conditions. For example, ASL is problematic when the transit time is long, as the method is limited by longitudinal (T_1) relaxation of the label. Bolus tracking MRI is commonly used to estimate perfusion, but blood brain barrier leakage in pathology can be a significant confound to CBF estimation. Hyperoxia perfusion mapping has its own nuances, many already discussed. Given that it uses the BOLD effect, it is insensitive to the transit time issues that impedes ASL. It also provides complimentary information to other hemodynamic techniques, such as: 1) measuring only the venous blood volume component (important for calibrated BOLD), 2) an extremely slow uptake

time relative to conventional techniques, which allows for more samples during the bolus passage, as well as the safety and patient comfort afforded by 3) using inhaled oxygen to generate a contrast bolus (as opposed to an injected contrast agent). Although we are using oxygen to alter the BOLD signal, the increased dissolved oxygen has a negligible effect on the extravascular tissue compared with the change in signal due to the deoxygenated hemoglobin change in the blood. This makes hyperoxia perfusion mapping unlike PET $^{15}O_2$ imaging where the oxygen in the tissue has the same effect as in the blood.

The tracer kinetics modeling approach described in the theory section is similar to the modeling approach used in DSC MRI. The use of indicator dilution theory requires several assumptions, particularly that the contrast does not exchange between the intra- and extra-vascular spaces. O_2, however, does exchange between these spaces, which would appear to violate this requirement, but the real contrast mechanism is from deoxyhemoglobin, which resides only in the blood. Furthermore, since the brain is always consuming oxygen, we have normalized the concentration functions to the baseline concentration of oxygen, so that the concentration functions represent only the extra oxygen given by the hyperoxia stimulus. We do not expect the $CMRO_2$ will be altered by this oxygen stimulus.

There are pros and cons to using the end-tidal oxygen values to estimate the AIF. An assumption is that the oxygen extraction fraction between the lungs and the arterial inputs to the brain is negligible. Measuring an AIF directly from the image data, as is done in DSC MRI, is appealing because it is direct. However, image-based measurement of the AIF also has many practical limitations, such as voxel selection sensitivity, partial voluming, low SNR, and limited temporal sampling. There is no concern about partial volume effects with the end-tidal estimation. The exponential model also fits the end-tidal values very well. Selecting a single imaging voxel as the AIF can often result in low SNR; this is ameliorated by selecting several voxels and averaging the outcome metric, but this can further increase the risk of partial volume errors. Although there have been some proposed automated methods for selecting the AIF from image data (Duhamel et al., 2006; Mouridsen et al., 2006), it is still often done manually which can be time consuming to an operator, but more worrisome is the sensitivity of the perfusion metrics to the choice of voxels selected to define the AIF. Using the end-tidal values to estimate the AIF avoids this issue as there is no user input required.

In conclusion, we have demonstrated a novel way to measure cerebral perfusion parameters with an inhaled oxygen passage, making it less invasive than other bolus passage imaging with injected contrast agents. CBF, CBV and MTT parameter maps show the expected gray matter and white matter contrast and ROI based measurements show values in agreement with known values in healthy participants. This approach may have applications in pathologies with long transit times and calibrated BOLD fMRI studies that include a hyperoxia challenge.

Acknowledgements

Appendix A. Supplementary data

Supplementary data related to this article can be found at https://doi.org/10.1016/j.neuroimage.2018.05.066.

References

Alsop, D.C., Detre, J.A., Golay, X., Günther, M., Hendrikse, J., Hernandez-Garcia, L., Lu, H., MacIntosh, B.J., Parkes, L.M., Smits, M., van Osch, M.J.P., Wang, D.J.J., Wong, E.C., Zaharchuk, G., 2015. Recommended implementation of arterial spin-labeled perfusion MRI for clinical applications: a consensus of the ISMRM perfusion study group and the European consortium for ASL in dementia. Magn. Reson. Med. 73, 102–116.

Baron, J.-C., Jones, T., 2012. Oxygen metabolism, oxygen extraction and positron emission tomography: historical perspective and impact on basic and clinical neuroscience. Neuroimage 61, 492–504.

Belliveau, J.W., Rosen, B.R., Kantor, H.L., Rzedzian, R.R., Kennedy, D.N., McKinstry, R.C., Vevea, J.M., Cohen, M.S., Pykett, I.L., Brady, T.J., 1990. Functional cerebral imaging by susceptibility-contrast NMR. Magn. Reson. Med. 14, 538–546.

Bengtsson, J., Bake, B., Johansson, Å., Bengtson, J.P., 2001. End-tidal to arterial oxygen tension difference as an oxygenation index. Acta Anaesthesiol. Scand. 45, 357–363.

Berman, A.J.L., Ma, Y., Hoge, R.D., Pike, G.B., 2016. The effect of dissolved oxygen on the susceptibility of blood. Magn. Reson. Med. 75, 363–371.

Blockley, N.P., Griffeth, V.E.M., Germuska, M.A., Bulte, D.P., Buxton, R.B., 2013. An analysis of the use of hyperoxia for measuring venous cerebral blood volume: comparison of the existing method with a new analysis approach. Neuroimage 72, 33–40.

Boxerman, J.L., Bandettini, P.A., Kwong, K.K., Baker, J.R., Davis, T.L., Rosen, B.R., Weisskoff, R.M., 1995. The intravascular contribution to fmri signal change: Monte Carlo modeling and diffusion-weighted studies in vivo. Magn. Reson. Med. 34, 4–10.

Buckley, D.L., 2002. Uncertainty in the analysis of tracer kinetics using dynamic contrast-enhanced T1-weighted MRI. Magn. Reson. Med. 47, 601–606.

Bulte, D.P., Chiarelli, P.A., Wise, R.G., Jezzard, P., 2006. Cerebral perfusion response to hyperoxia. J. Cerebr. Blood Flow Metabol. 27, 69–75.

Bulte, D.P., Kelly, M., Germuska, M., Xie, J., Chappell, M.A., Okell, T.W., Bright, M.G., Jezzard, P., 2012. Quantitative measurement of cerebral physiology using respiratory-calibrated MRI. Neuroimage 60, 582–591.

Buxton, R.B., 2009. Introduction to Functional Magnetic Resonance Imaging: Principles and Techniques. Cambridge University Press.

Calamante, F., Gadian, D.G., Connelly, A., 2000. Delay and dispersion effects in dynamic susceptibility contrast MRI: simulations using singular value decomposition. Magn. Reson. Med. 44, 466–473.

Chen, J.J., Pike, G.B., 2010. MRI measurement of the BOLD-specific flow-volume relationship during hypercapnia and hypocapnia in humans. Neuroimage 53, 383–391.

Chen, J.J., Smith, M.R., Frayne, R., 2005a. Advantages of frequency-domain modeling in dynamic-susceptibility contrast magnetic resonance cerebral blood flow quantification. Magn. Reson. Med. 53, 700–707.

Chen, J.J., Smith, M.R., Frayne, R., 2005b. The impact of partial-volume effects in dynamic susceptibility contrast magnetic resonance perfusion imaging. J. Magn. Reson. Imag. 22, 390–399.

Croal, P.L., Driver, I.D., Francis, S.T., Gowland, P.A., 2017. Field strength dependence of grey matter on venous oxygenation. Neuroimage 146, 327–332.

Cui, W., Zhu, X.-H., Vollmers, M.L., Colonna, E.T., Adriany, G., Tramm, B., Dubinsky, J.M., Oz, G., 2013. Non-invasive measurement of cerebral oxygen metabolism in the mouse brain by ultra-high field 17O MR spectroscopy. J. Cerebr. Blood Flow Metabol. 33, 1846–1849.

Davis, T.L., Kwong, K.K., Weisskoff, R.M., Rosen, B.R., 1998. Calibrated functional MRI: mapping the dynamics of oxidative metabolism. Proc. Natl. Acad. Sci. Unit. States Am. 95, 1834–1839.

Detre, J.A., Leigh, J.S., Williams, D.S., Koretsky, A.P., 1992. Perfusion imaging. Magn. Reson. Med. 23, 37–45.

Duhamel, G., Schlaug, G., Alsop, D.C., 2006. Measurement of arterial input functions for dynamic susceptibility contrast magnetic resonance imaging using echoplanar images: comparison of physical simulations with in vivo results. Magn. Reson. Med. 55, 514–523.

Frackowiak, R.S., Lenzi, G.-L., Jones, T., Heather, J.D., 1980. Quantitative measurement of regional cerebral blood flow and oxygen metabolism in man using 15O and positron emission tomography: theory, procedure, and normal values. J. Comput. Assist. Tomogr. 4, 727–736.

Gauthier, C.J., Hoge, R.D., 2012. Magnetic resonance imaging of resting OEF and CMRO2 using a generalized calibration model for hypercapnia and hyperoxia. Neuroimage 60, 1212–1225.

Grandin, C.B., Bol, A., Smith, A.M., Michel, C., Cosnard, G., 2005. Absolute CBF and CBV measurements by MRI bolus tracking before and after acetazolamide challenge: repeatabilily and comparison with PET in humans. Neuroimage 26, 525–535.

Grubb, R.L., Raichle, M.E., Eichling, J.O., Ter-Pogossian, M.M., 1974. The effects of changes in PaCO2 cerebral blood volume, blood flow, and vascular mean transit time. Stroke 5, 630–639.

Haddock, B., Larsson, H.B.W., Hansen, A.E., Rostrup, E., 2013. Measurement of brain oxygenation changes using dynamic T1-weighted imaging. Neuroimage 78, 7–15.

Hatazawa, J., Fujita, H., Kanno, I., Satoh, T., Iida, H., Miura, S., Murakami, M., Okudera, T., Inugami, A., Ogawa, T., Shimosegawa, E., Noguchi, K., Shohji, Y., Uemura, K., 1995. Regional cerebral blood flow, blood volume, oxygen extraction fraction, and oxygen utilization rate in normal volunteers measured by the autoradiographic technique and the single breath inhalation method. Ann. Nucl. Med. 9, 15–21.

Hoffmann, S.H., Radbruch, A., Bock, M., Semmler, W., Nagel, A.M., 2014. Direct 17O MRI with partial volume correction: first experiences in a glioblastoma patient. Magnetic Resonance Materials in Physics, Biology and Medicine 27, 579–587.

Hoge, R.D., Atkinson, J., Gill, B., Crelier, G.R., Marrett, S., Pike, G.B., 1999. Investigation of BOLD signal dependence on cerebral blood flow and oxygen consumption: the deoxyhemoglobin dilution model. Magn. Reson. Med. 42, 849–863.

Iscoe, S., Fisher, J.A., 2005. Hyperoxia-induced hypocapnia *: an underappreciated risk. Chest, p. 430+.

Ito, S., Mardimae, A., Han, J., Duffin, J., Wells, G., Fedorko, L., Minkovich, L., Katznelson, R., Meineri, M., Arenovich, T., Kessler, C., Fisher, J.A., 2008. Non-invasive prospective targeting of arterial P CO 2 in subjects at rest. J. Physiol. 586, 3675–3682.

Lee, T.Y., 2002. Functional CT: physiological models. Trends Biotechnol. 20, S3–S10.

Ma, Y., Berman, A.J., Pike, G.B., 2015. The effect of dissolved oxygen on the relaxation rates of blood plasma: implications for hyperoxia calibrated BOLD. Magn. Reson. Med.

MacDonald, M.E., Frayne, R., 2015. Cerebrovascular MRI: a review of state-of-the-art approaches, methods and techniques. NMR Biomed. 28, 767–791.

MacDonald, M.E., Smith, M.R., Frayne, R., 2011. Deconvolution with simple extrapolation for improved cerebral blood flow measurement in dynamic susceptibility contrast magnetic resonance imaging during acute ischemic stroke. Magn. Reson. Imag. 29, 620–629.

Mark, C.I., Fisher, J.A., Pike, G.B., 2011. Improved fMRI calibration: precisely controlled hyperoxic versus hypercapnic stimuli. Neuroimage 54, 1102–1111.

Mazziotta, J., Toga, A., Evans, A., Fox, P., Lancaster, J., Zilles, K., Woods, R., Paus, T., Simpson, G., Pike, B., Holmes, C., Collins, L., Thompson, P., MacDonald, D., Iacoboni, M., Schormann, T., Amunts, K., Palomero-Gallagher, N., Geyer, S., Parsons, L., Narr, K., Kabani, N., Goualher, G.L., Boomsma, D., Cannon, T., Kawashima, R., Mazoyer, B., 2001. A probabilistic atlas and reference system for the human brain: international Consortium for Brain Mapping (ICBM). Philos. Trans. R. Soc. Lond. Ser. B Biol. Sci. 356, 1293–1322.

Mouridsen, K., Christensen, S., Gyldensted, L., Østergaard, L., 2006. Automatic selection of arterial input function using cluster analysis. Magn. Reson. Med. 55, 524–531.

Ogawa, S., Lee, T.-M., Nayak, A.S., Glynn, P., 1990. Oxygenation-sensitive contrast in magnetic resonance image of rodent brain at high magnetic fields. Magn. Reson. Med. 14, 68–78.

Ogawa, S., Lee, T.M., Barrere, B., 1993. The sensitivity of magnetic resonance image signals of a rat brain to changes in the cerebral venous blood oxygenation. Magn. Reson. Med. 29, 205–210.

Østergaard, L., Sorensen, A.G., Kwong, K.K., Weisskoff, R.M., Gyldensted, C., Rosen, B.R., 1996a. High resolution measurement of cerebral blood flow using intravascular tracer bolus passages. Part II: experimental comparison and preliminary results. Magn. Reson. Med. 36, 726–736.

Østergaard, L., Weisskoff, R.M., Chesler, D.A., Gyldensted, C., Rosen, B.R., 1996b. High resolution measurement of cerebral blood flow using intravascular tracer bolus passages. Part I: mathematical approach and statistical analysis. Magn. Reson. Med. 36, 715–725.

Pike, G.B., 2012. Quantitative functional MRI: concepts, issues and future challenges. Neuroimage 62, 1234–1240.

Pilkinton, D.T., Gaddam, S.R., Reddy, R., 2011. Characterization of paramagnetic effects of molecular oxygen on blood oxygenation level-dependent-modulated hyperoxic contrast studies of the human brain. Magn. Reson. Med. 66, 794–801.

Pilkinton, D.T., Hiraki, T., Detre, J.A., Greenberg, J.H., Reddy, R., 2012. Absolute cerebral blood flow quantification with pulsed arterial spin labeling during hyperoxia corrected with the simultaneous measurement of the longitudinal relaxation time of arterial blood. Magn. Reson. Med. 67, 1556–1565.

Poulin, M.J., Liang, P.J., Robbins, P.A., 1996. Dynamics of the cerebral blood flow response to step changes in end-tidal PCO2 and PO2 in humans. J. Appl. Physiol. 81, 1084–1095.

Rempp, K.A., Brix, G., Wenz, F., Becker, C.R., Gückel, F., Lorenz, W.J., 1994. Quantification of regional cerebral blood flow and volume with dynamic susceptibility contrast-enhanced MR imaging. Radiology 193, 637–641.

Roberts, H.C., Roberts, T.P.L., Lee, T.-Y., Dillon, W.P., 2002. Dynamic, contrast-enhanced CT of human brain tumors: quantitative assessment of blood volume, blood flow, and microvascular permeability: report of two cases. Am. J. Neuroradiol. 23, 828–832.

Severinghaus, J.W., 1979. Simple, accurate equations for human blood O2 dissociation computations. J. Appl. Physiol. 46, 599–602.

Sourbron, S., Dujardin, M., Makkat, S., Luypaert, R., 2007. Pixel-by-pixel deconvolution of bolus-tracking data: optimization and implementation. Phys. Med. Biol. 52, 429.

Sourbron, S., Ingrisch, M., Siefert, A., Reiser, M., Herrmann, K., 2009. Quantification of cerebral blood flow, cerebral blood volume, and blood–brain-barrier leakage with DCE-MRI. Magn. Reson. Med. 62, 205–217.

Sourbron, S., Luypaert, R., Van Schuerbeek, P., Dujardin, M., Stadnik, T., Osteaux, M., 2004. Deconvolution of dynamic contrast-enhanced MRI data by linear inversion: choice of the regularization parameter. Magn. Reson. Med. 52, 209–213.

Sourbron, S.P., Buckley, D.L., 2011. On the scope and interpretation of the Tofts models for DCE-MRI. Magn. Reson. Med. 66, 735–745.

Tofts, P.S., 1997. Modeling tracer kinetics in dynamic Gd-DTPA MR imaging. J. Magn. Reson. Imag. 7, 91–101.

Tofts, P.S., Brix, G., Buckley, D.L., Evelhoch, J.L., Henderson, E., Knopp, M.V., Larsson, H.B.W., Lee, T.-Y., Mayr, N.A., Parker, G.J.M., Port, R.E., Taylor, J., Weisskoff, R.M., 1999. Estimating kinetic parameters from dynamic contrast-enhanced t1-weighted MRI of a diffusable tracer: standardized quantities and symbols. J. Magn. Reson. Imag. 10, 223–232.

Willats, L., Calamante, F., 2012. The 39 steps: evading error and deciphering the secrets for accurate dynamic susceptibility contrast MRI. NMR Biomed. 913–931.

Zaharchuk, G., Martin, A.J., Dillon, W.P., 2008. Noninvasive imaging of quantitative cerebral blood flow changes during 100% oxygen inhalation using arterial spin-labeling MR imaging. Am. J. Neuroradiol. 29, 663–667.

Zhu, X.-H., Chen, J.M., Tu, T.-W., Chen, W., Song, S.-K., 2013a. Simultaneous and noninvasive imaging of cerebral oxygen metabolic rate, blood flow and oxygen extraction fraction in stroke mice. Neuroimage 64, 437–447.

Zhu, X.-H., Zhang, Y., Wiesner, H.M., Ugurbil, K., Chen, W., 2013b. In vivo measurement of CBF using 17O NMR signal of metabolically produced H217O as a perfusion tracer. Magn. Reson. Med. 70, 309–314.